EXPERIMENTAL INVESTIGATION OF SOLUBILITY TRAPPING IN 3D PRINTED MICROMODELS

Alexandros Patsoukis Dimou[1,4,5] (iD), Mahdi Mansouri Boroujeni[2] (iD), Sophie Roman[3] (iD), Hannah P. Menke[1] (iD), Julien Maes[1] (iD)

[1]Institute of Geoenergy and Engineering, Heriot-Watt University, Edinburgh, UK; [2]Laboratoire de Chimie Bactérienne, CNRS-Aix Marseille University UMR7283, Institut de Microbiologie de la Méditerranée, Marseille, France; [3]Institut des Sciences de la Terre d'Orléans, Univ. Orléans, CNRS, BRGM, ISTO UMR 7327, Orléans, France; [4]Institute of Fluid Science, Tohoku University, Aoba Ward, Sendai, Miyagi, Japan; [5]School of Physics and Astronomy, University of Edinburgh, Edinburgh, UK

ABSTRACT

Understanding interfacial mass transfer during dissolution of gas in a liquid is vital for optimizing large-scale carbon capture and storage operations. While the dissolution of CO_2 bubbles in reservoir brine is a crucial mechanism towards safe CO_2 storage, it is a process that occurs at the pore-scale and is not yet fully understood. Direct numerical simulation (DNS) models describing this type of dissolution exist and have been validated with semi-analytical models on simple cases like a rising bubble in a liquid column. However, DNS models have not been experimentally validated for more complicated scenarios such as dissolution of trapped CO_2 bubbles in pore geometries where there are few experimental datasets. In this work, we present an experimental and numerical study of trapping and dissolution of CO_2 bubbles in 3D printed micromodel geometries. We used 3D printing technology to generate three different geometries, a single cavity geometry, a triple cavity geometry, and a multiple channel geometry. To investigate the repeatability of the trapping and dissolution experimental results, each geometry was printed three times, and three identical experiments were performed for each geometry. The experiments were performed at a low capillary number (Ca = 3.33 x 10^{-6}), representative of flow during CO_2 storage applications. The DNS simulations were then performed and compared with the experimental results. Our results show experimental reproducibility and consistency in terms of CO_2 trapping and the CO_2 dissolution process. At such a low capillary number, our numerical simulator cannot model the process accurately due to parasitic currents and the strong time-step constraints associated with capillary waves. However, we show that, for the single and triple cavity geometry, the interfacial transfer and resulting bubble dissolution can be reproduced by a numerical strategy where the interfacial tension is divided by 100 to relax the capillary time-step constraints. The full experimental dataset is provided and can be used to benchmark and improve future numerical models.

1. INTRODUCTION

Accurate prediction of gas dissolution during flow in porous media is vital for CO_2 storage applications (5, 28). During CO_2 storage, large quantities of the captured CO_2 are injected into the pore-space of an underground reservoir (e.g., saline aquifer, depleted oil and gas field) for permanent storage. Trapping of CO_2 can occur though four distinct mechanisms: **1) structural trapping**, where an impermeable cap rock restricts the CO_2 to escape the formation rock, **2) residual trapping**, where the CO_2 is trapped in disconnected clusters inside the reservoir rock, **3) solubility trapping**, where the CO_2 is dissolved inside the formation water and **4) mineral trapping**, which refers to the mineralization of CO_2 via reactions with minerals, aqueous phase, and organic matter inside the formation (53).

While we are mainly interested in the accurate prediction of storage at the reservoir scale (8, 15, 45), three of the four trapping mechanisms (residual, solubility, and mineral) primarily occur at the pore-scale. It is therefore crucial to accurately integrate these pore-scale mechanisms into reservoir-scale models, a process referred to as upscaling. Although the upscaling of residual trapping at the pore-scale has been extensively investigated (23, 31, 49), these investigations seldom include the effect of solubility trapping, mainly because numerical models of multiphase flow at the pore-scale that include interfacial transfer are not ready for simulations in micro-CT images at reservoir conditions.

Computational Fluid Dynamics (CFD) are an essential tool that complement experiments while allowing for sensitivity analysis of various physical parameters. Numerical simulations describing two-phase flow can be performed using the algebraic Volume-of-Fluid (VOF) method (50). In the VOF method, the interface between the two fluids is captured using an indicator function. Interface transfer can be modelled with the VOF method using a single-field approach and the Continuous Species Transfer (CST) method (19, 35). This method has been extended to simulate the local volume change resulting from the interfacial transfer, and used to successfully capture dissolution of a rising gas bubble in a liquid column (34). However, there is lack of an experimental dataset that allows benchmarking of the existing model during complicated scenarios where the fluid/solid interaction impacts the dissolution process, such as trapping CO_2 bubbles in a pore-space. Simulations of the dissolution of a single CO_2 bubble trapped in a single cavity have been performed (33, 38), but have not been experimentally validated. Multiphase flow in porous media is characterized by the capillary number, which is the ratio of viscous forces to capillary forces. Because the VOF suffers from the well-known problem of parasitic currents at low capillary numbers (Ca <10-5) (1) where capillary forces are dominant, the capability of the model to simulate gas bubbles dissolution at flow rates representative of CO_2 geological storage is unclear.

Micromodels are artificial replicas of natural porous media with standardized, repeatable geometries and have contributed to our understanding of pore-scale physics (12, 25, 43, 44, 46, 47). Micromodel experiments are advantageous because experiments can be conducted in the same geometry with multiple experimental protocols. Furthermore, they allow for geometric control of porous media and therefore enable the precise investigation of the impact of pore structure on flow. Due to their transparent nature, micromodels also permit direct fluid flow observation with a high-speed, high-resolution camera. Micromodels have thus been widely utilized to investigate physio-chemical phenomena in geoscience. Sun and Cubaud (48) used single channel microfluidics to investigate CO_2 bubble dissolution in water, ethanol, and methanol inside a channel. Microfluidic devices have been used to visualize convective mixing of CO_2 in water and n-decane (2). Furthermore, pore-scale scCO$_2$ dissolution experiments have been conducted in heterogeneous micromodels for both imbibition and

drainage processes (7, 9, 10, 11). However, micromodel fabrication techniques like etching and molding are slow, expensive, and limited in 2D and 2.5D structures. While microfabrication of micromodels with polydimethylsiloxane (PDMS) is inexpensive and allows for investigation of fluid flow, PDMS is permeable to gas (4, 27) and thus not suitable for studying CO_2 dissolution.

The emergence of additive manufacturing, also called 3D printing, allows for a compelling alternative to conventional micromodels. Three dimensional printing converts computer-assisted design (CAD) into a physical object in a single additive process. Commercial 3D printers, which can produce structures ranging from a few microns to several centimeters, are beginning to challenge conventional microfluidic fabrication techniques as the research prototyping approach to micro-fabrication (17). Three dimensional printing has been applied to a wide range of industries including medicine (51), biomedical engineering (3) and aerospace engineering (21). Compared with standard micromodel fabrication techniques, the attraction of 3D printing is twofold. First, 3D printing has the potential to fabricate in three dimensions in a way that was not previously possible. Secondly, the inexpensive nature of the 3D printed micromodels combined with the fast fabrication (~3 h) enables experimental investigations in multiple geometries quickly, allowing for optimization of the geometry that will produce the best experimental dataset (52) as well as geometrical sensitivity analysis. Two-dimensional single-layer 3D printed micromodels have already attracted attention and have been used to investigate pore-scale phenomena relevant to flow during subsurface processes (24, 29, 36, 37, 54). Three dimensional printed micromodels have also been experimentally validated as devices to conduct fluid flow experiments (39) and have been previously leveraged for water-CO_2 multiphase flow experiments (40).

In this paper we have two objectives: **1)** to investigate whether we can generate identical 3D printed microfluidic devices where trapping and dissolution of CO_2 can occur repeatably and generate a benchmark dataset; **2)** to investigate whether existing direct numerical simulations describing CO_2 dissolution can accurately capture the dissolution rate obtained from the experiments conducted in the 3D printed micromodels. The method for the micromodel generation is presented in Section 2. We then introduce the experimental apparatus in Section 3 and the image processing in Section 4. We present the numerical methods in Section 5 with the results and conclusions of this work in Sections 6 and 7.

2. MICROMODEL GENERATION

The 3D printed micromodel devices were designed with the use of the OpenSCAD [a] open-source software which meshes the structure into the stl format. Three identical microfluidic devices were printed for each of the three different geometries with increasing model complexity. The first geometry consists of a single cavity of 1 mm width and 2 mm height connected with single channel of 1 mm width (SC) (**Fig. 1A**). The second microfluidic design consists of 3
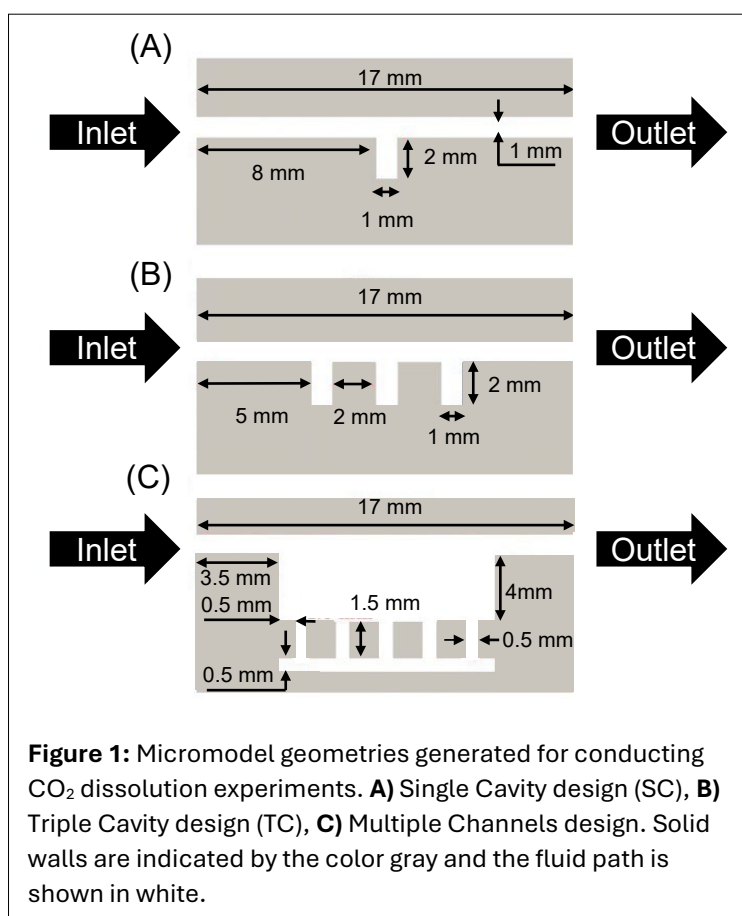

Figure 1: Micromodel geometries generated for conducting CO_2 dissolution experiments. **A)** Single Cavity design (SC), **B)** Triple Cavity design (TC), **C)** Multiple Channels design. Solid walls are indicated by the color gray and the fluid path is shown in white.
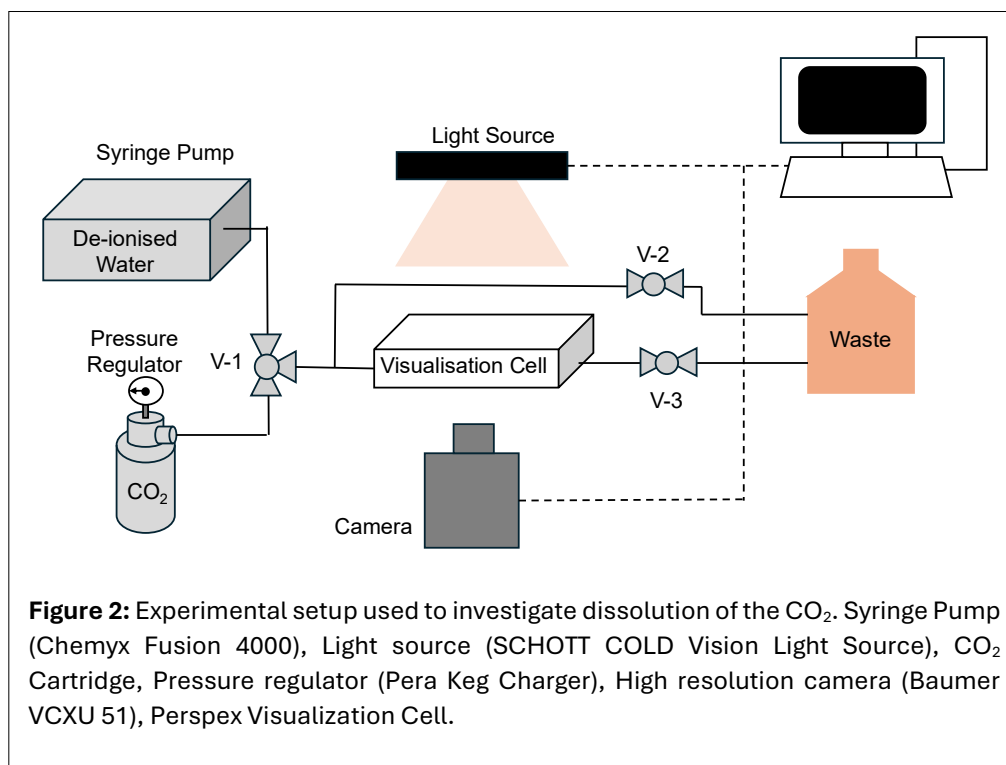
[a] *https://openscad.org/index.html*

cavities of 1 mm width and 2 mm height. The cavities are placed at a 2 mm distance from each other and connected with a single channel with 1 mm width (TC) (**Fig. 1B**). The third design consists of a top 4 mm channel connected perpendicularly via five 500 µm channels to a 500 µm bottom channel (MC) (**Fig. 1C**). The overall depth of the patterns was set to 1 mm for all micromodel designs. The micromodels were printed using the Formlabs Form 2 stereolithography (SLA) printer. Formlabs Form 2 works by successively solidifying layers of liquid photopolymer resin one on top of the other. The resin used for the generation of the micromodel devices is the Clear Resin provided by Formlabs. A detailed description of the printing process and the resolution of the printer can be found in Patsoukis-Dimou et al ([40]).

In the SC geometry **Figure 1A** the channel is connected to a single cavity which represents a single pore. For the TC geometries (**Fig. 1A, B**) the cavities where the CO_2 can be trapped are disconnected. This scenario represents a case where three different pores are connected on a single flow path. In the SC case, any trapped CO_2 will be dissolved directly into the injected pure water. However, in the TC case, dissolution in the first cavity will alter the CO_2 concentration in the water, potentially influencing the dissolution rates in the second and third cavities as the flow progresses. In both cases, we ensure that the trapped CO_2 can only dissolve and is not displaced by viscous or capillary forces. The MC geometry (**Fig. 1C**) consists of connected cavities therefore allowing for the possibility of the trapped CO_2 to be moved due to water displacement. The MC geometry not only allows for the possibility to investigate the dissolution process upon trapping, but also the ability to investigate the combination of multiphase flow displacement combined with the dissolution process.

3. EXPERIMENTAL SETUP

The printed micromodel was inserted in the Perspex transparent visualization cell face-down and sealed using an O-ring. PEEK tubing with a diameter of 1/16-inch was used to connect the syringe pump[b] and a pressure regulator[c] to a three-way valve with 1/16-inch peek tubing to the bypass, visualization cell, and then to the outlet. A high-resolution camera[d] which allowed for a 3.45 µm/pixel resolution was

Figure 2: Experimental setup used to investigate dissolution of the CO_2. Syringe Pump (Chemyx Fusion 4000), Light source (SCHOTT COLD Vision Light Source), CO_2 Cartridge, Pressure regulator (Pera Keg Charger), High resolution camera (Baumer VCXU 51), Perspex Visualization Cell.

---

mounted beneath the flow cell and recorded images using the Stream Pix 11 software[e]. Above the visualization cell, an LED light source[f] was installed to reduce shadows and enable clear visualization of the fluid movement. The experimental setup can be seen in **Figure 2**. A detailed schematic of the Perspex visualization cell can be found in the **Supporting Material** (available online).

For each experiment, pure CO_2 was injected into the system for 10 minutes by imposing a pressure differential of 3.7 Pa with a total of over 200 pore volumes (PV) injected through the system to ensure full saturation of the micromodel with CO_2 and removal of any air in the system. Distilled water was then injected inside the micromodel at constant flow rate and the trapping and dissolution of CO_2 was recorded with the high-resolution camera at an acquisition speed of 1 frame per second. A flow rate of Q = 1.67 x10^{-10} m^3.s^{-1} was used for all experiments. During CO_2 storage, CO_2 is injected into the reservoir and displaces the brine. Once the injection stops, water imbibition occurs as brine re-enters the pore spaces due to capillary forces trapping the CO_2 in pores. During this process, the trapped CO_2 gradually dissolves in the surround-ding water, a mechanism referred to as dissolution trapping. Our approach replicates this process, allowing us to study trapp-ed CO_2 dissolution in a controlled manner. The experiments were carried out at atmospheric pressure (0.10 MPa) and room temperature conditions (20°C).

Figure 3: A) Raw image of the channel -cavity system obtained with a high resolution camera. **B)** Conceptual image explaining the inability to observe the curvature of the interface between the water and CO_2 phase at the Z axis. Due to this inability, the fraction of CO_2 corresponding to the middle plane (shaded) is measured. **C)** Raw image and **D)** segmented image of the cavity.

4. IMAGE PROCESSING

Images were post-processed in MATLAB® to improve the image quality. First, the images were denoised using contrast limited adaptive histogram equalization (22), followed by the adaptive wiener denoise filter (30), and then any remaining artifacts were removed manually. The pore-space was then segmented, and the water, solid and CO_2 phases were separated using a watershed algorithm based on the grayscale intensity of each pixel. Finally, the pixels representing the CO_2 phase were counted in every successive image. Due to the inability to observe the curvature of the trapped bubbles in the Z axis, the pixels measured in every successive image represent the fraction of CO_2 in the middle plane as demonstrated in **Figure 3**.

---

[e] *https://www.norpix.com/products/streampix/streampix.php*

[f] *SCHOTT ColdVision Light Source: https://www.schott.com/de-de/lighting-and-imaging?gclsrc=aw.ds&gad_source=1&gad_campaignid=9720444650&gclid=CjwKCAjwravBBhBjEiwAIr30VPWmMJE7VOIdFdB9Kf6QuPVD35-dtm0f46inXGu6FCfk_JeVTVyFVhoCz7MQAvD_BwE*

5. NUMERICAL METHODS

In this work, the numerical simulation of two-phase flow is performed using the algebraic Volume-of-Fluid (VOF) method for which the interface between the two fluids is captured using an indicator function. To transport the indicator function, an advection equation is numerically solved. Interface transfer is modelled within the VOF method (20) by using the single-field approach and the Continuous Species Transfer (CST) method (18, 35). In the single-field approach, a mixture quantity, obtained through volume averaging of species concentration, is transported by solving an algebraic equation. With our model, it is assumed that each phase is Newtonian and incompressible, and any gravity forces are neglected. Furthermore, it is assumed that the gas phase is pure. The governing equations solved are provided in detail in the **Supporting Material** (available online).

In this system of equations, the relative importance of all mechanisms at play is quantified by three dimensionless numbers. These are the Reynolds number (**Eq. 1**), which is the ratio of inertial forces to viscous forces, the Péclet number (**Eq. 2**), which is the ratio of advection to diffusion, and the Capillary number (**Eq. 3**), which is the ratio of viscous to capillary forces.

$$Re = \frac{\rho_1 \boldsymbol{U} L}{\mu_1}, \tag{1}$$

$$Pe = \frac{\boldsymbol{U} L}{D_1}, \tag{2}$$

$$Ca = \frac{\mu_1 \boldsymbol{U}}{\sigma}, \tag{3}$$

In **Equations 1**, **2** and **3**, $\boldsymbol{U}$ is the reference velocity (m.s-1) which is the velocity inside the inlet channel for the SC, TC and MC geometry. Subscript 1 in **Equations 1**, **2** and **3** indicates the aqueous phase. L is the characteristic length (m), which is the width of the inlet channel. ρ_1 is the density of the aqueous phase (kg.m-3). μ_1 is the viscosity of the aqueous phase (Pa.s). D_1 is the diffusion coefficient (m2.s-1), and σ is the surface tensions (N.m-1).

In reality, as CO_2 dissolves in the water phase, it dissociates into H+ and HCO_3-. Nevertheless, in our simulation framework, we neglect any chemical reactions, and we assume a single component bubble where only one species exists in the CO_2 phase, which can be transferred to the water phase. The fluid properties for the water and the CO_2 used in this work are summarized in **Table 1**. The dimensionless numbers Re, Pe and Ca for the three geometries are 0.17, 104.17 and 3.33x10^{-6}, respectively.

The capillary numbers obtained in the experiments are as low as Ca = 3.33x10^{-6}. Direct numerical simulation of multiphase flow at such a low capillary number is challenging for two reasons. The presence of parasitic currents is a well-known challenge (6, 16, 26, 41, 42). Parasitic currents are located close to the fluid-fluid interface, and in our case, can impact on the volume of the CO_2 that will be trapped inside the cavity during the displacement, and the dissolution of the gas phase once it has been trapped. Additionally, the propagation of capillary waves imposes a stability time-step constraint known as the capillary wave or Brackbill time-step constraint (6) (**Eq. 4**) where Δx is the grid block size (m) and ρ_1 and ρ_2 are the density of the aqueous phase and the CO_2 phase respectively.

$$\Delta t < \Delta t_B = \sqrt{\frac{(\rho_1 + \rho_2)\Delta x^3}{4\pi\sigma}} \tag{4}$$

For the fluid properties presented in **Table 1**, and for a mesh resolution Δx = 50 μm, we obtain Δt_B = 1.17 x10^{-5}. Therefore, to simulate an injection time of 5 mins would require 2.55 x10^{7} time-steps, and the computational time would be too restrictive.

One possible way to simulate the experiments conducted in the SC and the TC geometries is by initializing the bubbles inside the cavities, and to only simulate the dissolution of the bubbles after they

Phase	Density (kg.m-3)	Dynamic Viscosity (Pa.s)	Henry's Constant (-)	Interfacial tension (mN.m-1)	Diffusion Coefficient in water (m².s⁻¹)
Table 1: Fluid properties for CO_2 and water (13, 14).					
CO_2	1.87	1.5×10^{-5}	1.25	-	1.6×10^{-9}
Water	1000	10^{-3}	0	72	-

have been trapped with a reduced surface tension of $\sigma/100$. Indeed, if the bubbles always remain at capillary equilibrium, the value of the interfacial tension does not impact the flow behavior. To ensure that the bubbles remain at capillary equilibrium, the pressure inside the bubbles is monitored and compared to the capillary pressure obtained using the Young-Laplace equation (**Eq. 5**) where θ is the contact angle (°) and r is the effective radius of the interface (m).

$$P_c = \frac{2\sigma cos\theta}{r} \tag{5}$$

Using this method, a DNS simulation can be performed for the SC and TC geometries. However, a DNS simulation for the MC geometry cannot be conducted. This is because in the MC geometry, the dissolution of the CO_2 is coupled with displacement of the CO_2. Such a process is strongly affected by the surface tension, and therefore reducing the surface tension would lead to erroneous results. Furthermore, due to the increased complexity and size of the domain, the mesh size is larger than the rest of the scenarios making the computational time significantly higher, and thus the simulation was not performed.

The numerical method has been implemented in GeoChemFoam[9] following the work of Maes and Soulaine (34). To mesh the computational domain, a 3D uniform cartesian grid was first generated, and then cells containing solid were removed and replaced by cartesian cells to match the solid boundaries using the OpenFOAM snappyHexMesh utility. Given the size of the computational domain, a mesh with a cell resolution of 50x50 µm was used. The flow rates used for the simulations are the same as the flow rates used for the experiments. To satisfy the Brackbill time-step constraint, the time-step used is $\Delta t = 1 \times 10^{-4}$ s. All numerical simulations are performed in parallel in 24 core processors leading to a CPU-hour usage of 47 hours for the SC geometry and 75 hours for the TC geometry.

Finally, as a comparison with the experiments, we extracted and measured the fraction of CO_2 that occupies the middle plane inside the cavity of the DNS 3D geometry, which is what is measured in experiments conducted with 3D printed micromodels, and compared it with the DNS results. This workflow is demonstrated for the SC geometry in **Figure S1** in the **Supplementary Material** (available online).

To assess the repeatability of the experimental results, the Coefficient of Variance (CV) is used. The CV of the experimental results is calculated as follows (**Eq. 6**),

$$CV = \frac{\sigma}{\overline{CO_{2ex}}} \tag{6}$$

where $\overline{CO_{2ex}}$ is the mean experimental value and σ the standard deviation (-) calculated as (**Eq. 7**),

$$\sigma = \sqrt{\frac{\sum_{i=0}^{k}(CO_{2ex(i)} - \overline{CO_{2ex}})^2}{n}} \tag{7}$$

---

[9] *https://github.com/geochemfoam*

where k is the number of the experiments (-), $CO_{2_{ex\,(i)}}$ is the fraction of CO_2 measured at experiment i (-) and n is the point in time.

Finally, the overall error between the average experimental values and the direct numerical simulation is calculated as (**Eq. 8**),

$$\epsilon = \frac{1}{n}\sum_{t=0}^{n}\left|\frac{\overline{CO_{2_{ex}}} - CO_{2_{DNS}}}{\overline{CO_{2_{ex}}}}\right| \qquad (8)$$
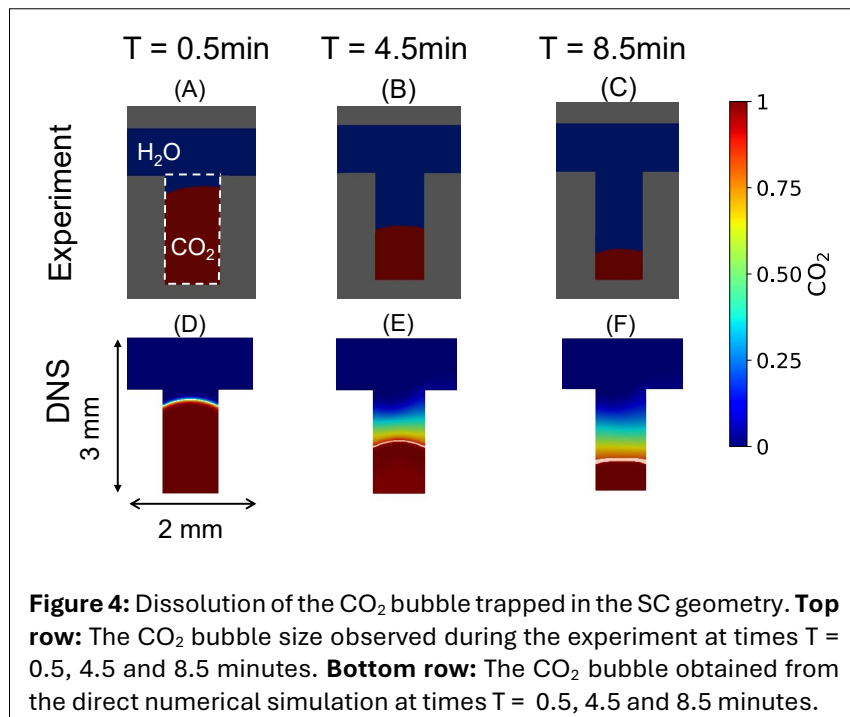
where $CO_{2_{DNS}}$ is the fraction of CO_2 calculated with the DNS (-).
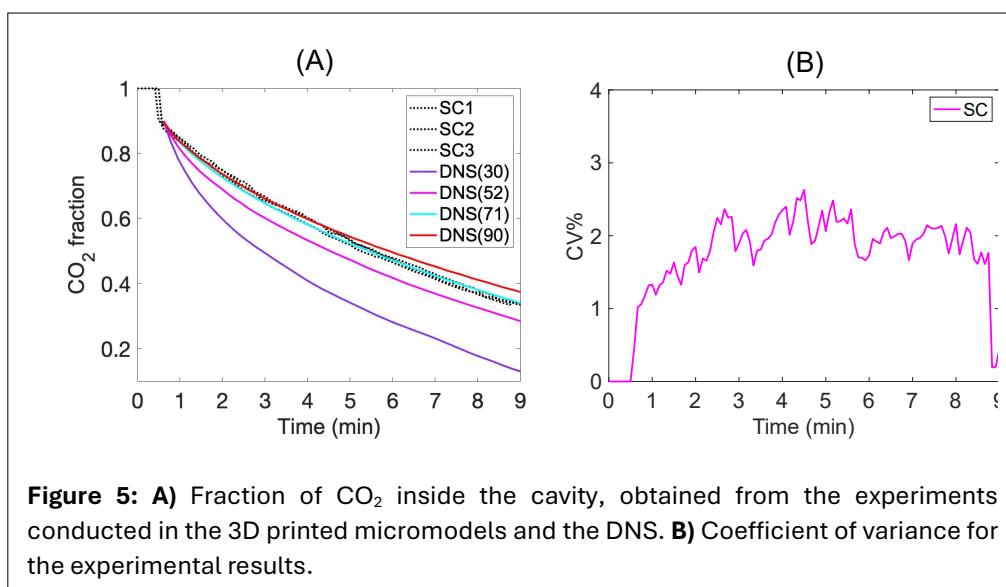
6. RESULTS & DISCUSSION

Three CO_2 trapping and dissolution experiments were performed in various geometries and the repeatability of the trapping and dissolution of the CO_2 in each geometry was investigated. Direct numerical simulation of the dissolution of the CO_2 was then performed to investigate whether DNS can accurately capture the experimental results.

6.1. Single cavity configuration

Three experiments were conducted in three identical SC micromodel geometries. The fraction of CO_2 inside the cavity was measured. The area can be seen in white in **Figure 4A**. Until the moment water entered the cavity, it was fully saturated with CO_2, and the fraction was unity. In all experiments at T = 0.5 min, water invaded the cavity and trapped the CO_2. The fraction of CO_2 trapped inside the cavity was 0.89 for experiment SC1, 0.90 for experiment SC2, and 0.88 for experiment SC3, leading to a variation of 2% between the experiments. Once the CO_2 was trapped in the cavity, only the disso-

Figure 4: Dissolution of the CO_2 bubble trapped in the SC geometry. **Top row:** The CO_2 bubble size observed during the experiment at times T = 0.5, 4.5 and 8.5 minutes. **Bottom row:** The CO_2 bubble obtained from the direct numerical simulation at times T = 0.5, 4.5 and 8.5 minutes.

lution process occurred. The overall change of the CO_2 inside the cavity is shown in **Figure 4** and **Figure 5A**. All experiments show the same trend of dissolution rate for the CO_2 bubble inside the cavity. After T = 9 min, when the trapped CO_2 volume had become significantly reduced, the bubble underwent a rearrangement, resulting in a sudden increase in the measured CO_2 fraction. This change may be attributed to the bubble detaching from one of the walls and migrating as a result of buoyancy forces. Further details are provided in the **Supporting Material** (available online).
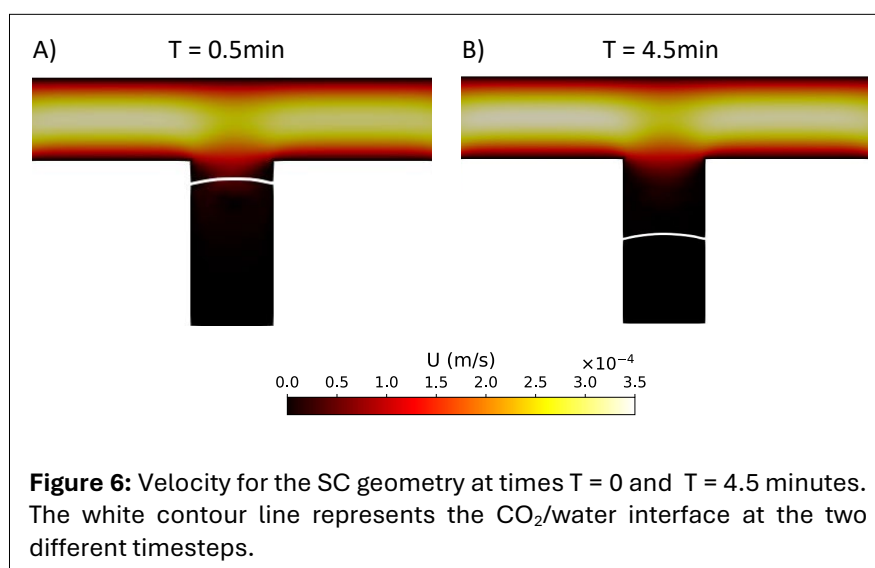
The CO_2 initially dissolved at a high rate but decreased with time. This may be because initially, the CO_2/water interface is located near the main channel, where the higher velocity makes advection more influential. As the CO_2 bubble dissolves, the CO_2/water interface moves away from the channel and the advection has a reduced impact on the dissolution processes of the CO_2. This can be seen in **Figure 6**. In **Figure 5B**, the temporal evolution of the CV is shown. Here, the CV remains below 3%, indicating good repeatability of the experimental process. This demonstrates that the 3D-printed single-cavity

Figure 5: A) Fraction of CO_2 inside the cavity, obtained from the experiments conducted in the 3D printed micromodels and the DNS. **B)** Coefficient of variance for the experimental results.

geometry can be consistently reproduced, enabling reliable two-phase flow and dissolution experiments. The small error could be due to artificial roughness, which is not repeatable in different prints, however, the reproducibility provides confidence that the results could be used to validate direct numerical simulation models.

For the DNS benchmark simulation, the bubble was initialized inside the cavity so that the fraction of CO_2 was 0.89, matching the bubble size trapped in the experiments. Initially, water injection and CO_2 dissolution were disabled, allowing the CO_2 to equilibrate under capillary and gravity forces. At T = 0.5 min, dissolution of the CO_2 was enabled, and pure water was injected in the left side of the channel at a flow rate of Q = 1.67 x10^{-10} $m^3.s^{-1}$, which is Ca = 3.33 x10^{-6}. To identify the contact angle that should be used in the direct numerical simulation, 20 contact angles measurements were manually performed on the experiment images using image processing software[h]. The average value of the contact angles measured was 71°.

To test the impact of the contact angle in the dissolution of the bubble, two further simulations were run where the contact angle was set to 30°, 52° and 90° degrees. The results of the numerical simulation can be seen in **Figure 4** and **Figure 5A**. When comparing the numerical simulation results to the experimental results at times T = 0.5, 4.5 and 8.5 min, we observe that the numerical simulation that most accurately captures the mass evolution of the CO_2 bubble is the one where the contact angle is set to 71°. Furthermore, increasing the contact angle to 90° has little impact to the dissolution of the CO_2 bubble, whereas decreasing the contact angle to 52° has a significant impact on the CO_2 dissolution. Finally, when the contact angle was set to 30° degrees, there was a large deviation between the simulation and the experimental results. *The non-linear increase of the CO_2 dissolution rate*
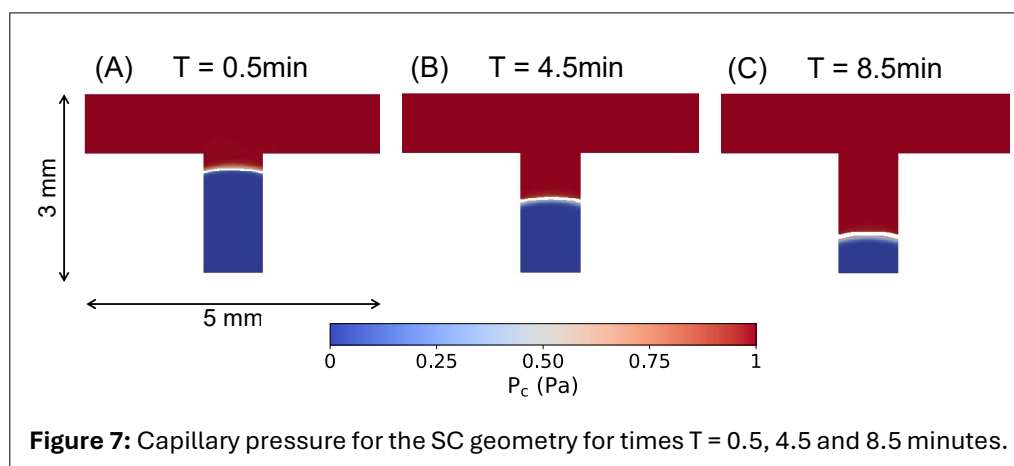

Figure 6: Velocity for the SC geometry at times T = 0 and T = 4.5 minutes. The white contour line represents the CO_2/water interface at the two different timesteps.

[h] *Fiji ImageJ:* *https://imagej.net/software/fiji/*

observed with a decreasing contact angle from 90° is possibly due to the increased interfacial area between the CO_2 and the water. In **Figure 5A**, it can also be seen that the numerical results are within the range of experimental observations until time T = 6 min, indicating an initially accurate prediction of the dissolution of the CO_2 bubble. After this point, the DNS results start to diverge from the experimental results.

Our method is first-order accurate (38), and satisfies the Brackbill constraint, ensuring stability. The divergence between the DNS and the experimental results could be attributed to several factors: numerical errors caused by parasitic currents, insufficient mesh resolution leading to a lack of numerical convergence, or inaccuracies in the transport parameters H and D. The overall error between the numerical simulation and the average experimental is ε = 1%. To further investigate the reason for deviation would require improvement of the computational efficiency of the solver and reduction of the large time-step restrictions.

Figure 7 shows the capillary pressure at times T = 0.5, 4.5 and 8.5 min. The capillary pressure stays constant at a value of P_c = 1 Pa, which indicates that the bubble is at capillary equilibrium. Therefore, the surface tension does not impact the dissolution of the CO_2 bubble, which is consistent with our assumption, and shows that performing the simulation with a reduced surface tension of $\sigma/100$ does not impact the simulation results. Finally, as shown in **Figure 5A**, the contact angle has a significant impact on the dissolution of the trapped bubble. and when the contact angle is set to 90° and 30° degrees, the simulation fails to capture the dissolution observed in the experimental results accurately. A decrease in the contact angle leads to an increase in the surface area between the CO_2 and water phase, allowing for faster dissolution.

Figure 7: Capillary pressure for the SC geometry for times T = 0.5, 4.5 and 8.5 minutes.
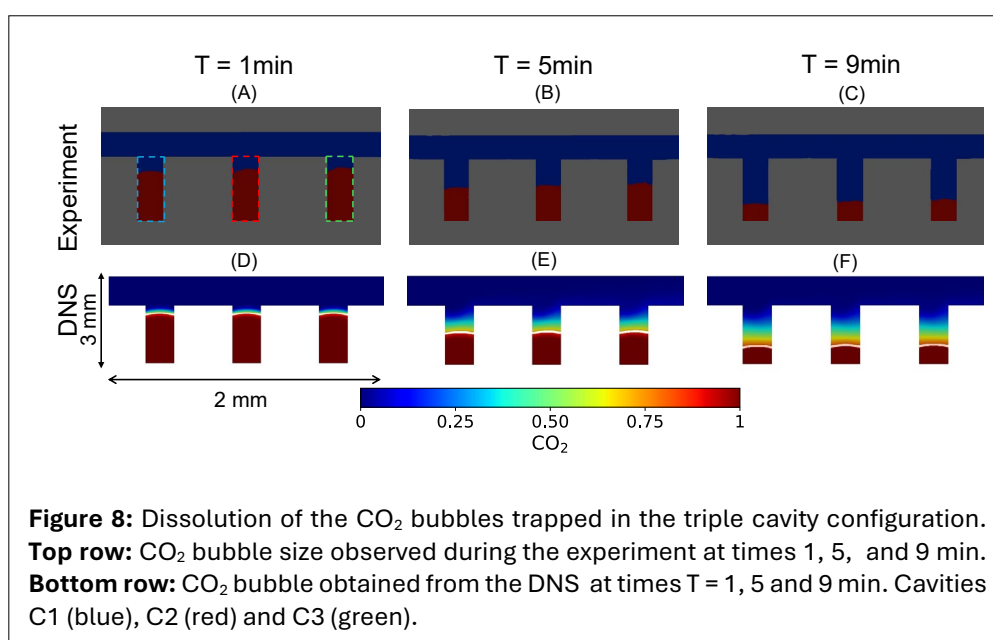
6.2. Triple cavity configuration

Three experiments were conducted in three identical triple cavity (TC) micromodel geometries. In all three experiments at time T = 0.4 min, water trapped the CO_2 in the first cavity (TC_C1), at T = 0.7 min in the second cavity (TC_C2), and T = 1 min in the third cavity (TC_C3). The amount of CO_2 trapped in each cavity and the error ε between the amount of CO_2 trapped in each cavity between different experiments can be seen in **Table 2**. The experimental results show that the amount of CO_2 trapped inside the cavities is the same between the identical experiments with an error of 2%. In **Figures 8** and **9A** we can observe the overall change of the CO_2 fraction inside the three cavities. Across all three experiments, the extent of CO_2 trapping and subsequent bubble dissolution were consistently reproducible, as indicated by CV values below 3% for all cavities (**Fig. 9B**), underscoring the repeatability of the experimental process. **Figure 9A** also shows that, as in the SC case, the dissolution rate decreases over time, indication that the process is more strongly influenced by advection when the water/CO_2 interface is close to the main channel.

In the DNS simulation, the bubbles were initialized inside the cavities so that the fraction of CO_2 in the middle plane matched the fraction of CO_2 trapped in the experiments conducted in the 3D printed

Table 2: Fraction of CO_2 inside the cavities for the experiment conducted in the TC geometries.

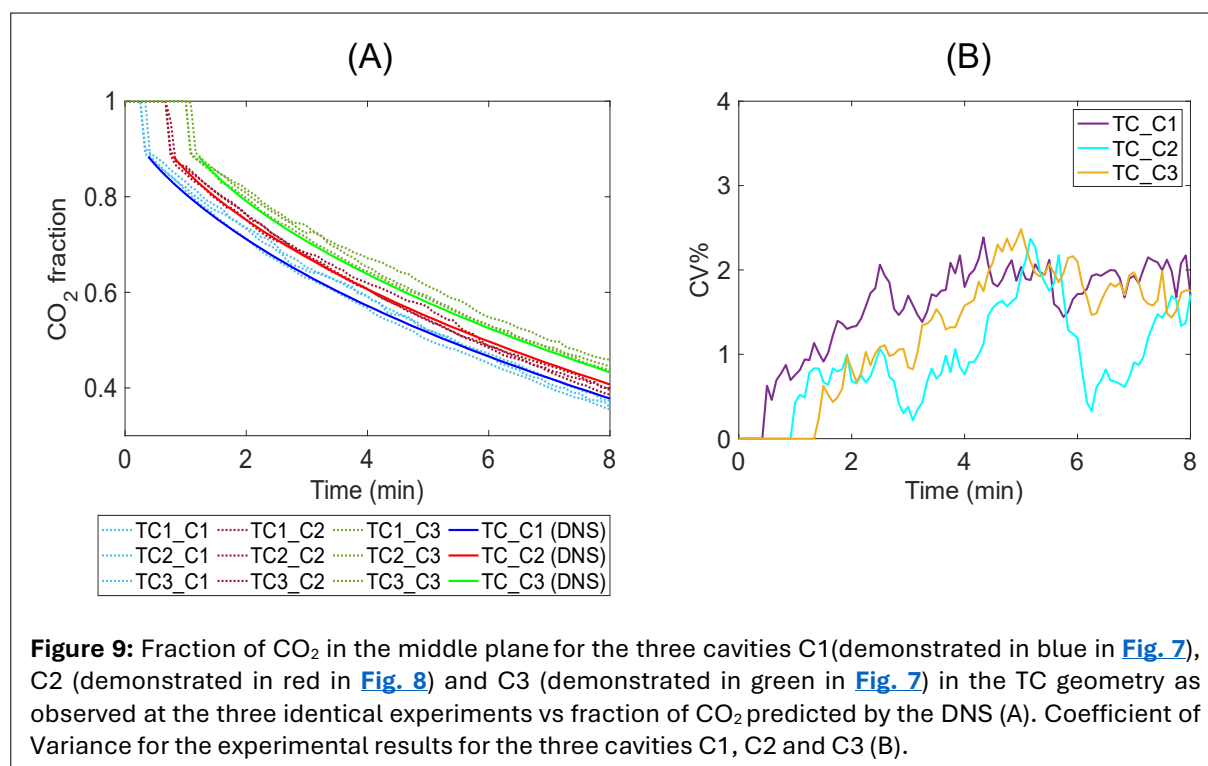| Geometry	Trapped CO_2 TC1	Trapped CO_2 TC2	Trapped CO_2 TC3	Error
TC_C1	0.90	0.89	0.88	2%
TC_C2	0.89	0.87	0.87	2%
TC_C3	0.88	0.89	0.89	1%

micromodels. The contact angle was set to 71°. At T = 0, pure water was injected in the left side of the channel at a flow rate Q = 1.67 x10^{-10} m^3.s^{-1} and Ca = 3.33 x10^{-6}. The results of the numerical simulation can be seen in **Figure 7** and **Figure 8**. During the dissolution of the bubble at times T = 1, 5 and 9 min, the numerical simulation accurately captured the mass evolution of the CO_2 bubbles. In **Figure 8**, it can also be seen that the dissolution rate predicted by the numerical simulation matches the dissolution rate obtained from the experiments conducted in 3D printed micromodels. The overall average error between the average experimental values and the direct numerical simulation for the three cavities is ε_{C1} = 1.81%, ε_{C2} = 1.86%, and ε_{C3} = 2.52%. For the first (C1) and second cavity (C2), we observed an increased deviation

Figure 8: Dissolution of the CO_2 bubbles trapped in the triple cavity configuration. **Top row:** CO_2 bubble size observed during the experiment at times 1, 5, and 9 min. **Bottom row:** CO_2 bubble obtained from the DNS at times T = 1, 5 and 9 min. Cavities C1 (blue), C2 (red) and C3 (green).
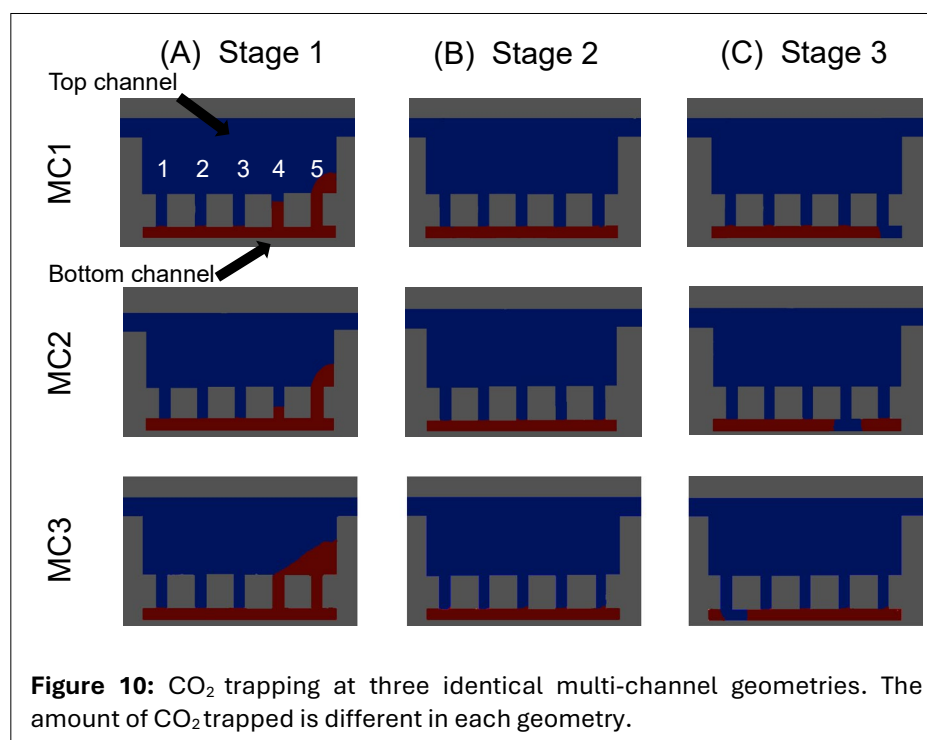
between the simulation and experimental results after 4 and 6 minutes respectively. This deviation was not observed for the third cavity in the time frame of our experiment. For the third cavity (C3), the increased overall error between the numerical and experimental results (ε_{C3} = 2.52%) could be due to experimental error, or because the dissolution process had already begun during the injection phase—resulting in partially CO_2-saturated water by the time it reached C3, after trapping CO_2 in the first (C1) and second (C2) cavities. This would lead to a decrease in the concentration gradient between the water and the trapped CO_2 in the third cavity, which would result in a slower dissolution process as observed in the experiments. Initializing the bubbles inside the cavity does not consider the aforementioned process, introducing error into the overall system. As for the simulation results in SC, investigating this error further will require improving the computational efficiency of the solver.

6.3.   Multiple Channels

Three experiments were conducted in the MC geometry. The experimental results can be seen in **Figure 10**. In **Figure 10**, the experiments in the three micromodels were separated into three Stages. In Stage 1, the initial amount of CO_2 trapped inside the three identical micromodels when the injected water reaches the outlet can be seen. Here the amount of trapped CO_2 is different inside the three identical micromodels, which could possibly be due to artificial surface roughness being different in the three

Figure 9: Fraction of CO_2 in the middle plane for the three cavities C1(demonstrated in blue in **Fig. 7**), C2 (demonstrated in red in **Fig. 8**) and C3 (demonstrated in green in **Fig. 7**) in the TC geometry as observed at the three identical experiments vs fraction of CO_2 predicted by the DNS (A). Coefficient of Variance for the experimental results for the three cavities C1, C2 and C3 (B).

micromodel devices. While this was also true in the previous cases, in the MC case, where water can propagate through multiple pathways, the effect of surface roughness is more pronounced. As a result, surface roughness leads to greater variability in fluid displacement and trapping compared to the simpler SC and TC cases. In Stage 2, as the CO_2 dissolved inside the top channel and the five perpendicular channels, the only CO_2 in the geometries was in the bottom channel. Finally, in Stage 3, as the dissolution continued, the water invaded the bottom channel of the geometry. The bottom channel was invaded by channel 4 in the MC1 experiment, and by channel 5 in the MC2 experiment, and by channel 1 in the MC3 experiment. As the trapped CO_2 phase dissolved, the water phase advanced and invaded the bottom channels. The invasion of the bottom channel from Stage 2 to Stage 3 strongly depends on the capillary entry pressure.

Figure 10: CO_2 trapping at three identical multi-channel geometries. The amount of CO_2 trapped is different in each geometry.

The different pattern of invasion observed at the bottom channel in the three experiments also indicates that there is artificial roughness impacting the flow displacement. Artificial surface roughness can result in one of the perpendicular channels having a different effective entry pressure than the rest. This throat size difference can simultaneously impact the capillary entry pressure of the throat as well as the dissolution rate, which leads to a preferential pathway during the invasion of the water in the geometry. In homogeneous cases like the MC geometry, where the five perpendicular channels have the same width, the displacement is strongly affected by small inconsistencies and artificial roughness. Moreover, at Stage 3, the saturation of CO_2 as well as the interface area is different for the three different experiments. The maximum amount of trapping is 89% (MC1) of the bottom channel, while the minimum is 84% (MC3), resulting in a 6% variation between the experiments. Furthermore, the interfacial area is approximately 3 mm^2 for MC1 and MC3, while for MC2 it is around 2.5 mm^2. This lack of repeatability in water evolution makes the MC geometry a poor benchmark dataset, limiting its suitability for robust comparison and validation of the numerical simulator. The 3D printed micromodel design specifications for achieving repeatable single phase flow experiments have been previously investigated (40). However, further investigations are required into the design specifications under which repeatable multiphase flow experiments can be performed in 3D printed micromodels.

Furthermore, conducting a direct numerical simulation using a reduced surface tension is not possible in this case as the dissolution is coupled with displacement of the CO_2. Using a different surface tension would significantly impact the simulation results. Furthermore, the mesh size is significantly larger and would lead to increased computational time beyond what is feasible for this study.

7. CONCLUSIONS

For this work, we used 3D printing technology to generate three micromodel geometries: the single cavity (SC), triple cavity (TC), and multiple channels geometry (MC). We printed each geometry three times and conducted CO_2 trapping and dissolution experiments to assess the repeatability of experiments in each geometry. The experimental results showed that in the cases of the SC and the TC geometries, the trapping is repeatable for all three experiments with an error of 2%. Comparison of the temporal evolution of the CO_2 in the three SC micromodels showed similar results. Moreover, comparisons of the temporal evolution of the CO_2 inside the three TC geometries also showed reproducible results. In all experiments conducted in the SC and TC geometries, we initially observed a fast dissolution rate which decreased as the bubble dissolves. While previous works have utilized micromodel devices to investigate trapping and dissolution of CO_2 (10, 11), this is the first experimental work that provides repeatable results where CO_2 bubbles are trapped and dissolved under known boundary conditions. The known boundary conditions during the experiment allowed for direct comparison with DNS. For the MC geometry, the initial trapping and dissolution pattern differed between different experiments. This could be due to the surface roughness affecting the trapping pattern. Surface roughness present in an otherwise homogeneous system, like the MC geometry, can have a strong impact on the flow progression. Thus, the experimental results obtained for the MC geometry cannot be used as a benchmark dataset. *To be able to study the simultaneous displacement and dissolution between miscible phases, improved 3D printing surface quality will be required which will render possible generation of micromodels where the surface roughness is repeatable.*

The capillary number for experiments conducted in the SC and TC geometries is *Ca* = 3.33x10^{-6}. The low capillary number does not allow for performing accurate direct numerical simulation due to spurious currents. Therefore, to simulate the phenomenon for the single and triple cavity configurations, we initialized the bubble inside the cavity and simulated only the dissolution process of the experiment using a surface tension of $\sigma/100$. This limitation prevented accurate simulation of bubble trapping, as surface tension has a strong influence on fluid displacement. However, it still allows for the calculation of CO_2 dissolution within the SC and TC geometries by initializing the bubbles inside the cavity. For the SC geometry, DNS accurately captured the dissolution and matched the experimental results obtained from the 3D printed micromodels. For the TC model, the DNS also accurately captured the dissolution for the first (C1) and the second cavities (C2). We observed a small deviation manifesting for the third

cavity. That could be because, in the experiment, as water flows toward the third cavity (C3), dissolution has already begun in the first (C1) and second cavities (C2), partially increasing the CO_2 concentration in the water. This led to a decrease in the concentration gradient between the water phase and the CO_2 trapped in the third cavity (C3), and a slower dissolution of the CO_2 bubble. This phenomenon cannot be captured with the DNS, where the bubbles are initialized in the cavities.

Development of the numerical models to capture capillary dominated processes for multiphase flow that overcome existing problems, such as capillary waves and spurious currents, is required (33). With this work, we produced an experimental dataset that allowed for validation of numerical models that capture multiphase flow displacement with interfacial transfer of a gas to an aqueous phase. Finally, we showed that although simple scenarios like the dissolution of CO_2 in a simple cavity can be accurately captured, faster computational methods capable of solving low capillary number scenarios in more complicated geometries are needed to be able to calculate CO_2 dissolution in a complicated rock pore-space scenario accurately. Our study's findings contribute to the development of highly precise predictive models for understanding the behavior of trapped CO_2 in the pore-space. The accurate prediction of CO_2 behavior and dissolution processes in the pore-space, combined with effective upscaling to the core scale, has the potential to significantly enhance our ability to extract reliable core-scale data. This will allow for developing more effective CO_2 storage strategies, helping mitigate greenhouse gas emissions.

STATEMENTS AND DECLARATIONS

Supplementary Material
Supplementary material for this paper is available and can be downloaded here.

Author Contributions
APD: Conceptualization, Formal analysis, Writing - original draft, review & editing, Data curation, Validation, Visualization, Software, Investigation. **HPM:** Conceptualization, Writing - review & editing, Supervision, Project administration. **JM:** Conceptualization, Writing - review & editing, Supervision, Funding acquisition, Project administration, Software. **SR:** Conceptualization, Writing - review & editing, Supervision, Funding acquisition, Project administration. **MMB:** Conceptualization, investigation, Writing - review & editing.

Conflicts of Interest
The authors declare that they have no known competing financial interests or personal relationships that could have appeared to influence the work reported in this paper.

Data, Code & Protocol Availability
The experimental dataset and the micromodel geometries can be found at the Open Science Framework (OSF) repository https://osf.io/gfvm5/.

ORCID IDs

Alexandros Patsoukis Dimou	🆔 https://orcid.org/0000-0002-0625-7865
Mahdi Mansouri Boroujeni	🆔 https://orcid.org/0009-0003-9570-6283
Sophie Roman	🆔 https://orcid.org/0000-0001-9168-3449
Hannah Menke	🆔 https://orcid.org/0000-0002-1445-6354
Julien Maes	🆔 https://orcid.org/0000-0002-3248-9758

REFERENCES

1. Abadie, T., Aubin, J., & Legendre, D. (2015). On the combined effects of surface tension force calculation and interface advection on spurious currents within Volume of Fluid and Level Set frameworks. *Journal of Computational Physics*, 297, 611-636. https://doi.org/https://doi.org/10.1016/j.jcp.2015.04.054

2. Amarasinghe, W., Farzaneh, S., Fjelde, I., Sohrabi, M., & Guo, Y. (2021). A Visual Investigation of CO_2 Convective Mixing in Water and Oil at the Pore Scale Using a Micromodel Apparatus at Reservoir Conditions. *Gases*, 1(1), 53-67. https://doi.org/10.3390/gases1010005

3. Beg, S., Almalki, W. H., Malik, A., Farhan, M., Aatif, M., et al. (2020). 3D printing for drug delivery and biomedical applications. *Drug Discovery Today*, 25(9), 1668-1681. https://doi.org/https://doi.org/10.1016/j.drudis.2020.07.007

4. Berean, K., Ou, J. Z., Nour, M., Latham, K., McSweeney, C., et al. (2014). The effect of crosslinking temperature on the permeability of PDMS membranes: Evidence of extraordinary CO_2 and CH_4 gas permeation. *Separation and Purification Technology*, 122, 96-104. https://doi.org/https://doi.org/10.1016/j.seppur.2013.11.006

5. Black, J. R., Carroll, S. A., & Haese, R. R. (2015). Rates of mineral dissolution under CO_2 storage conditions. *Chemical Geology*, 399, 134-144. https://doi.org/https://doi.org/10.1016/j.chemgeo.2014.09.020

6. Brackbill, J. U., Kothe, D. B., & Zemach, C. (1992). A continuum method for modeling surface tension. *Journal of Computational Physics*, 100(2), 335-354. https://doi.org/https://doi.org/10.1016/0021-9991(92)90240-Y

7. Buchgraber, M., Kovscek, A. R., & Castanier, L. M. (2012). A Study of Microscale Gas Trapping Using Etched Silicon Micromodels. *Transport in Porous Media*, 95(3), 647-668. https://doi.org/10.1007/s11242-012-0067-0

8. Celia, M. A., Bachu, S., Nordbotten, J. M., & Bandilla, K. W. (2015). Status of CO_2 storage in deep saline aquifers with emphasis on modeling approaches and practical simulations. *Water Resources Research*, 51(9), 6846-6892. https://doi.org/https://doi.org/10.1002/2015WR017609

9. Chang, C., Zhou, Q., Kneafsey, T. J., Oostrom, M., & Ju, Y. (2019). Coupled supercritical CO_2 dissolution and water flow in pore-scale micromodels. *Advances in Water Resources*, 123, 54-69. https://doi.org/https://doi.org/10.1016/j.advwatres.2018.11.004

10. Chang, C., Zhou, Q., Kneafsey, T. J., Oostrom, M., Wietsma, T. W., & Yu, Q. (2016). Pore-scale supercritical CO_2 dissolution and mass transfer under imbibition conditions. *Advances in Water Resources*, 92, 142-158. https://doi.org/https://doi.org/10.1016/j.advwatres.2016.03.015

11. Chang, C., Zhou, Q., Oostrom, M., Kneafsey, T. J., & Mehta, H. (2017). Pore-scale supercritical CO_2 dissolution and mass transfer under drainage conditions. *Advances in Water Resources*, 100, 14-25. https://doi.org/https://doi.org/10.1016/j.advwatres.2016.12.003

12. Chen, Z., Xu, J., & Wang, Y. (2019). Gas-liquid-liquid multiphase flow in microfluidic systems – A review. *Chemical Engineering Science*, 202, 1-14. https://doi.org/https://doi.org/10.1016/j.ces.2019.03.016

13. Crank, J. (1975). The Mathematics of Diffusion (n. Edition, Ed.). Oxford University Press, London

14. Espinoza, D. N., & Santamarina, J. C. (2010). Water-CO_2-mineral systems: Interfacial tension, contact angle, and diffusion—Implications to CO_2 geological storage. *Water Resources Research*, 46(7). https://doi.org/https://doi.org/10.1029/2009WR008634

15. Fan, Y., Durlofsky, L. J., & Tchelepi, H. A. (2012). A fully-coupled flow-reactive-transport formulation based on element conservation, with application to CO2 storage simulations. *Advances in Water Resources*, 42, 47-61. https://doi.org/https://doi.org/10.1016/j.advwatres.2012.03.012

16. Francois, M. M., Cummins, S. J., Dendy, E. D., Kothe, D. B., Sicilian, J. M., & Williams, M. W. (2006). A balanced-force algorithm for continuous and sharp interfacial surface tension models within a volume tracking framework. *Journal of Computational Physics*, 213(1), 141-173. https://doi.org/https://doi.org/10.1016/j.jcp.2005.08.004

17. Gonzalez, G., Roppolo, I., Pirri, C. F., & Chiappone, A. (2022). Current and emerging trends in polymeric 3D printed microfluidic devices. *Additive Manufacturing*, 55, 102867. https://doi.org/https://doi.org/10.1016/j.addma.2022.102867

18. Graveleau, M., Soulaine, C., & Tchelepi, H. A. (2017). Pore-Scale Simulation of Interphase Multicomponent Mass Transfer for Subsurface Flow. *Transport in Porous Media*, 120(2), 287-308. https://doi.org/10.1007/s11242-017-0921-1

19. Haroun, Y., Legendre, D., & Raynal, L. (2010). Volume of fluid method for interfacial reactive mass transfer: Application to stable liquid film. *Chemical Engineering Science*, 65(10), 2896-2909. https://doi.org/https://doi.org/10.1016/j.ces.2010.01.012

20. Hirt, C. W., & Nichols, B. D. (1981). Volume of fluid (VOF) method for the dynamics of free boundaries. *Journal of Computational Physics*, 39(1), 201-225. https://doi.org/https://doi.org/10.1016/0021-9991(81)90145-5

21. Joshi, S. C., & Sheikh, A. A. (2015). 3D printing in aerospace and its long-term sustainability. *Virtual and Physical Prototyping*, 10(4), 175-185. https://doi.org/10.1080/17452759.2015.1111519

22. Karel, Z. (1994). Contrast Limited Adaptive Histogram Equalization. *Graphics Gems*, 0, 474-485. https://cir.nii.ac.jp/crid/1571698601099987968

23. Kohanpur, A. H., Rahromostaqim, M., Valocchi, A. J., & Sahimi, M. (2020). Two-phase flow of CO_2-brine in a heterogeneous sandstone: Characterization of the rock and comparison of the lattice-Boltzmann, pore-network, and direct numerical simulation methods. *Advances in Water Resources*, 135, 103469. https://doi.org/https://doi.org/10.1016/j.advwatres.2019.103469

24. Konno, M., Patsoukis Dimou, A., & Suzuki, A. (2023). Using 3D-printed fracture networks to obtain porosity, permeability, and tracer response datasets. *Data in Brief*, 47, 109010. https://doi.org/https://doi.org/10.1016/j.dib.2023.109010

25. Kuhn, S., & Jensen, K. F. (2012). A pH-Sensitive Laser-Induced Fluorescence Technique To Monitor Mass Transfer in Multiphase Flows in Microfluidic Devices. *Industrial & Engineering Chemistry Research*, 51(26), 8999-9006. https://doi.org/10.1021/ie300978n

26. Lafaurie, B., Nardone, C., Scardovelli, R., Zaleski, S., & Zanetti, G. (1994). Modelling Merging and Fragmentation in Multiphase Flows with SURFER. *Journal of Computational Physics*, 113(1), 134-147. https://doi.org/https://doi.org/10.1006/jcph.1994.1123

27. Lamberti, A., Marasso, S. L., & Cocuzza, M. (2014). PDMS membranes with tunable gas permeability for microfluidic applications. *RSC Advances*, 4(106), 61415-61419. https://doi.org/10.1039/C4RA12934B

28. Levine, J. S., Goldberg, D. S., Lackner, K. S., Matter, J. M., Supp, M. G., & Ramakrishnan, T. S. (2014). Relative Permeability Experiments of Carbon Dioxide Displacing Brine and Their Implications for Carbon Sequestration. *Environmental Science & Technology*, 48(1), 811-818. https://doi.org/10.1021/es401549e

29. Li, H., & Zhang, T. (2019). Imaging and characterizing fluid invasion in micro-3D printed porous devices with variable surface wettability. *Soft Matter*, 15(35), 6978-6987. https://doi.org/10.1039/C9SM01182J

30. Lim, J. S. (1990). Two-dimensional signal and image processing. Prentice Hall, Englewood Cliffs, N.J., ©1990.

31. Liu, H., Valocchi, A. J., Werth, C., Kang, Q., & Oostrom, M. (2014). Pore-scale simulation of liquid CO_2 displacement of water using a two-phase lattice Boltzmann model. *Advances in Water Resources*, 73, 144-158. https://doi.org/https://doi.org/10.1016/j.advwatres.2014.07.010

32. Maes, J., & Menke, H. P. (2021). GeoChemFoam: Direct Modelling of Multiphase Reactive Transport in Real Pore Geometries with Equilibrium Reactions. *Transport in Porous Media*, 139(2), 271-299. https://doi.org/10.1007/s11242-021-01661-8

33. Maes, J., & Menke, H. P. (2021). GeoChemFoam: Operator Splitting based time-stepping for efficient Volume-Of-Fluid simulation of capillary-dominated two-phase flow. arXiv:2105.10576 [physics.flu-dyn]. https://doi.org/10.48550/arXiv.2105.10576

34. Maes, J., & Soulaine, C. (2020). A unified single-field Volume-of-Fluid-based formulation for multi-component interfacial transfer with local volume changes. *Journal of Computational Physics*, 402, 109024. https://doi.org/https://doi.org/10.1016/j.jcp.2019.109024

35. Marschall, H., Hinterberger, K., Schüler, C., Habla, F., & Hinrichsen, O. (2012). Numerical simulation of species transfer across fluid interfaces in free-surface flows using OpenFOAM. *Chemical Engineering Science*, 78, 111-127. https://doi.org/https://doi.org/10.1016/j.ces.2012.02.034

36. Osei-Bonsu, K., Grassia, P., & Shokri, N. (2017). Investigation of foam flow in a 3D printed porous medium in the presence of oil. *Journal of Colloid and Interface Science*, 490, 850-858. https://doi.org/https://doi.org/10.1016/j.jcis.2016.12.015

37. Osei-Bonsu, K., Grassia, P., & Shokri, N. (2018). Effects of Pore Geometry on Flowing Foam Dynamics in 3D-Printed Porous Media. *Transport in Porous Media*, 124(3), 903-917. https://doi.org/10.1007/s11242-018-1103-5

38. Patoukis Dimou, A., & Maes, J. (2020, October 12-14). Volume-of-Fluid Simulation of Gas Dissolution in Liquid: Rising Bubbles and CO_2 Trapping. 14th International Conference of CFD in Oil & Gas, Metallurgical and Process Industries SINTEF, Trondheim, Norway. https://sintef.brage.unit.no/sintef-xmlui/handle/11250/2720857

39. Patsoukis Dimou, A., Menke, H. P., & Maes, J. (2022). Benchmarking the Viability of 3D Printed Micromodels for Single Phase Flow Using Particle Image Velocimetry and Direct Numerical Simulations. Transport in Porous Media, 141(2), 279-294. https://doi.org/10.1007/s11242-021-01718-8

40. Patsoukis Dimou, A., Suzuki, A., Menke, H. P., Maes, J., & Geiger, S. (2021). 3D printing-based microfluidics for Geosciences ICFD 2021 https://www.researchgate.net/publication/358426572_3D_printing-based_microfluidics_for_Geosciences

41. Prodanović, M., & Bryant, S. L. (2006). A level set method for determining critical curvatures for drainage and imbibition. *Journal of Colloid and Interface Science*, 304(2), 442-458. https://doi.org/https://doi.org/10.1016/j.jcis.2006.08.048

42. Renardy, Y., & Renardy, M. (2002). PROST: A Parabolic Reconstruction of Surface Tension for the Volume-of-Fluid Method. *Journal of Computational Physics*, 183(2), 400-421. https://doi.org/https://doi.org/10.1006/jcph.2002.7190

43. Roman, S., Soulaine, C., AlSaud, M. A., Kovscek, A., & Tchelepi, H. (2016). Particle velocimetry analysis of immiscible two-phase flow in micromodels. *Advances in Water Resources*, 95, 199-211. https://doi.org/https://doi.org/10.1016/j.advwatres.2015.08.015

44. Roman, S., Soulaine, C., & Kovscek, A. R. (2020). Pore-scale visualization and characterization of viscous dissipation in porous media. *Journal of Colloid and Interface Science*, 558, 269-279. https://doi.org/https://doi.org/10.1016/j.jcis.2019.09.072

45. Shariatipour, S. M., Pickup, G. E., & Mackay, E. J. (2016). Simulations of CO_2 storage in aquifer models with top surface morphology and transition zones. *International Journal of Greenhouse Gas Control*, 54, 117-128. https://doi.org/https://doi.org/10.1016/j.ijggc.2016.06.016

46. Shui, L., Eijkel, J. C. T., & van den Berg, A. (2007). Multiphase flow in microfluidic systems – Control and applications of droplets and interfaces. *Advances in Colloid and Interface Science*, 133(1), 35-49. https://doi.org/https://doi.org/10.1016/j.cis.2007.03.001

47. Soulaine, C., Maes, J., & Roman, S. (2021). Computational Microfluidics for Geosciences [Review]. *Frontiers in Water*, 3. https://doi.org/10.3389/frwa.2021.643714

48. Sun, R., & Cubaud, T. (2011). Dissolution of carbon dioxide bubbles and microfluidic multiphase flows. *Lab on a Chip*, 11(17), 2924-2928. https://doi.org/10.1039/C1LC20348G

49. Tahmasebi, P., Sahimi, M., Kohanpur, A. H., & Valocchi, A. (2017). Pore-scale simulation of flow of CO_2 and brine in reconstructed and actual 3D rock cores. *Journal of Petroleum Science and Engineering*, 155, 21-33. https://doi.org/10.1016/j.petrol.2016.12.031

50. Ubbink, O., & Issa, R. I. (1999). A Method for Capturing Sharp Fluid Interfaces on Arbitrary Meshes. *Journal of Computational Physics*, 153(1), 26-50. https://doi.org/https://doi.org/10.1006/jcph.1999.6276

51. Vukicevic, M., Mosadegh, B., Min, J. K., & Little, S. H. (2017). Cardiac 3D Printing and its Future Directions. *JACC: Cardiovascular Imaging*, 10(2), 171-184. https://doi.org/doi:10.1016/j.jcmg.2016.12.001

52. Waheed, S., Cabot, J. M., Macdonald, N. P., Lewis, T., Guijt, R. M., Paull, B., & Breadmore, M. C. (2016). 3D printed microfluidic devices: enablers and barriers. *Lab on a Chip*, 16(11), 1993-2013. https://doi.org/10.1039/C6LC00284F

53. Zhang, D., & Song, J. (2014). Mechanisms for Geological Carbon Sequestration. *Procedia IUTAM*, 10, 319-327. https://doi.org/https://doi.org/10.1016/j.piutam.2014.01.027

54. Zhang, J., Tuohey, J., Amini, N., Morton, D. A. V., & Hapgood, K. P. (2021). Liquid imbibition into 3D printed porous substrates. *Chemical Engineering Science*, 245, 116967. https://doi.org/https://doi.org/10.1016/j.ces.2021.116967